Photoacoustics 25 (2022) 100327

Contents lists available at ScienceDirect

Photoacoustics

journal homepage: www.elsevier.com/locate/pacs

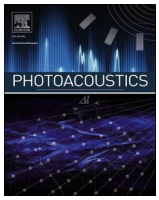

Quick identification of prostate cancer by wavelet transform-based photoacoustic power spectrum analysis

Shiying Wu [a,1], Ying Liu [b,1], Yingna Chen [a,c], Chengdang Xu [b], Panpan Chen [a], Mengjiao Zhang [a], Wanli Ye [a], Denglong Wu [b], Shengsong Huang [b,*], Qian Cheng [a,c,**]

[a] Institute of Acoustics, School of Physics Science and Engineering, Tongji University, Shanghai, PR China
[b] Department of Urology, Tongji Hospital, Tongji University School of Medicine, Shanghai, PR China
[c] Shanghai Research Institute for Intelligent Autonomous Systems, Tongji University, Shanghai, PR China

ARTICLE INFO

Keywords:
Photoacoustic measurement
Wavelet transform
Photoacoustic power spectrum analysis
ResNet-18 network
Prostate cancer grading

ABSTRACT

Pathology is currently the gold standard for grading prostate cancer (PCa). However, pathology takes considerable time to provide a final result and is significantly dependent on subjective judgment. In this study, wavelet transform-based photoacoustic power spectrum analysis (WT-PASA) was used for grading PCa with different Gleason scores (GSs). The tumor region was accurately identified via wavelet transform time-frequency analysis. Then, a linear fitting was conducted on the photoacoustic power spectrum curve of the tumor region to obtain the quantified spectral parameter *slope*. The results showed that high GSs have small glandular cavity structures and higher heterogeneity, and consequently, the *slopes* at both 1210 nm and 1310 nm were high ($p < 0.01$). The classification accuracy of the PA time frequency spectrum (PA-TFS) of tumor region using ResNet-18 was 89% at 1210 nm and 92.7% at 1310 nm. Further, the testing time was less than 7 mins. The results demonstrated that identification of PCa can be rapidly and objectively realized using WT-PASA.

1. Introduction

Recently, prostate cancer (PCa) has become the most commonly diagnosed cancer in men, accounting for 10% of all new male cancers worldwide [1,2]. For an American man, the lifetime risk of developing PCa is approximately 42% [3]. In particular, PCa has a high incidence but variable aggressiveness. PCa is curable and grows slowly in its early stage; however, when it becomes more aggressive, it is impossible to treat it, and the fatality rate is extremely high [4]. Therefore, grading PCa is crucial for reducing fatality rates. Currently, magnetic resonance (MRI) / ultrasound (US) guided biopsy puncture pathology is regarded as the "gold standard" that confirm the diagnosis of cancer as well as to classify tumor aggressiveness [5,6]. During the procedure, 16- or 18-gauge biopsy needles are used to extract 15 mm biopsy needle strips from the prostate tissue [7]. Each biopsied tissue can be graded according to the glandular cavity architecture and assigned a Gleason score (GS) [8,9]. Clinical studies have shown that in order to achieve better sensitivity to aggressive PCa, transperineal saturated biopsies sometimes will be conducted on more than 50 sites in one sample [10,11]; however, they cause great physical and mental pain to patients. Moreover, the pathology depends on the subjective judgment of the pathologist. Thus, the initial biopsy can only produce 80% accuracy diagnoses [10,11]. In addition, pathology is very time-consuming; it normally takes three–four days to obtain the results. US and MRI methods have shown great potential in PCa detection [12–14]; however, they focus on tissue whole morphology regardless of the distribution of the information of the glandular cavity structure [12–15], which is not consistent with the evaluation characteristics of the Gleason system. Therefore, a new method that can assess the aggressiveness of PCa more quickly, objectively and accurately is urgently required.

Photoacoustic (PA) detection is an emerging technology with the dual advantages of high sensitivity and high resolution. Its most important advantage lies in its ability to simultaneously evaluate the chemical and physical properties of tissues [16–18]. Photoacoustic power spectrum analysis (PASA), which analyzes the PA signal in the frequency domain, has demonstrated the capability of assessing the

* Corresponding author.
** Corresponding author at: Institute of Acoustics, School of Physics Science and Engineering, Tongji University, Shanghai, PR China.
E-mail addresses: hssfline@tongji.edu.cn (S. Huang), q.cheng@tongji.edu.cn (Q. Cheng).
[1] These authors contributed equally to this study.

https://doi.org/10.1016/j.pacs.2021.100327
Received 27 July 2021; Received in revised form 14 December 2021; Accepted 17 December 2021
Available online 18 December 2021

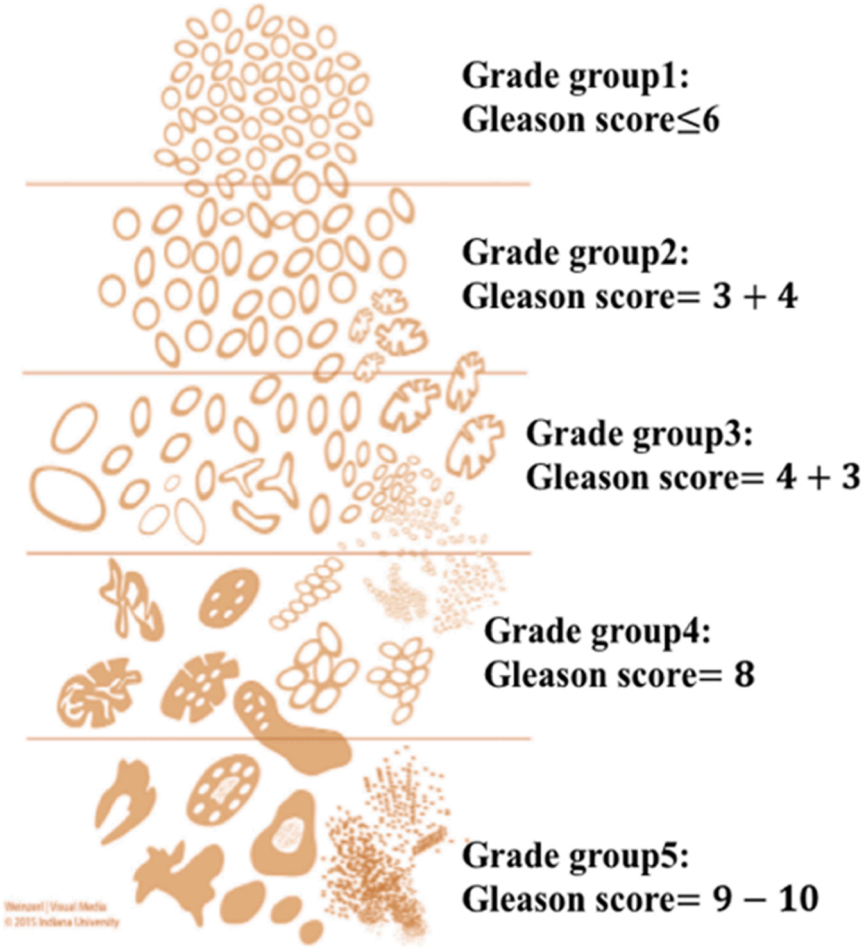

Fig. 1. Newly modified Gleason grading diagram presented in the ISUP publication [50].

size/microstructure of different chemical components in biological tissues [19–24], which is consistent with the evaluation characteristics of the Gleason system. According to the characteristics of different diseases, different spectral parameters are extracted to quantify changes in the chemical components of the lesion. Previous studies used different PA spectral parameters to study vascular diseases [25] and bone health [26–28] as well as to identify cancer [22,23,29–31]. In our previous study, we conducted PASA on the entire effective signal; this is because the PA spectral parameter *slope* indicates the proportion of the high- and low-frequency components of the entire effective signal generated by whole biological tissue [23,24,29–31]. However, the prostate biopsy core is different from other samples and has a 15 mm biopsy needle strip; in general, only 20–30% (approximately 4 mm) is tumor region, and the rest is normal prostate tissue [6–9]. In such a situation, the *slope* reflects the average structure size of the tissue, including the normal region; thus, causing inaccurate results [23,24,29–31]. To remove the influence of the normal region on the *slope* parameter, the tumor region must be selected first before PASA.

The continuous wavelet transform (CWT) can be used to simultaneously provide the joint distribution information of the time and frequency domains of PA signals [32]. The CWT technique has been applied in numerous fields, including cardiovascular health assessment [33–35], instrument fault detection [36,37], and geophysics [38,39]. In PA research, the CWT technique has been applied to assess bone health via evaluation of the frequency-related propagation attenuation of different bone samples [28,40]. Using CWT, we can acquire the distribution of frequency information along the 15 mm biopsy needle strip. Because the difference between PCa and normal tissue lies in the structural size of the glandular cavity, we can remove the influence of normal tissues by utilizing the frequency difference between the structure of a normal tissue and PCa using CWT.

Convolution neural networks (CNNs) are a type of deep feedforward neural network with convolution computation [41]. It is one of the representative algorithms of deep learning. Based on their rich representation power, fast inference, and filter sharing properties, CNNs have significantly increased the performance of image classification [42–45] and super-resolution reconstruction [46–48]. The deep residual network (ResNet) is one of the most commonly convolution CNNs. The core of the ResNet model is to establish “shortcuts” (skip connections) between the front and back layer, which is conducive to the backpropagation of gradients during training, so as to train a deeper CNN network and achieve higher accuracy [49]. ResNets (ResNet-18, ResNet-34, ResNet-50, ResNet-101, and ResNet-152, whose main difference lies in the number of network layers) perform better in image classification than other CNN models in ImageNet dataset, which indicate that image features could be well extracted by ResNets [49]. The performance of ResNet-18 is similar to other ResNets, which can retain more low-scale features owing to the reason that it is shallow. Therefore, we want to use ResNet-18 for the intelligent grading PCa.

In this study, we investigated a new method using wavelet transform-based photoacoustic power spectrum analysis (WT-PASA) to evaluate the aggressiveness of PCa via an *ex vivo* experiment on human prostate biopsy needle strip with different GSs. First, we conducted CWT time-frequency analysis on each sample to acquire the tumor region of the entire biopsy needle strip. Then, a linear fitting was conducted on the PA power spectrum curve of the tumor region to obtain the quantified

Table 1
Sample size.

Method	Normal	GS= 6	GS= 7	GS= 8
PASA (samples)	34	10	6	6
ResNet-18 (images)	340	100	60	60

spectral parameter *slope*. In addition, we employed ResNet-18 on the PA time-frequency spectrum (PA-TFS) images of tumor region to directly evaluate the aggressiveness of PCa. The total testing time was less than 7 mins (including 3 mins for PA detection, 2 mins for post-processing time, and 1 min for decision-making). The objective was to grade different GSs through the characterization of the microstructure of chemical content in the frequency spectrum.

2. Materials and methods

2.1. Human prostate biopsy needle strip

Four types of human PCa needle strips with a total of 56 samples, including benign (34 samples), GS = 6 (10 samples), GS = 7 (6 samples), and GS = 8 (6 samples), were collected in 2019–2021. All participants provided their informed consent, and all procedures were approved by the Institutional Review Committee of Tongji Hospital. According to the new modified Gleason grading diagram, as shown in Fig. 1 [50], when GS≤6, the cells are well differentiated and the structural differences are similar to those in normal tissues. In addition, it is indicated that patients with GS≥7 are more vulnerable to extraprostatic extension and biochemical recurrence [8,51]. Therefore, three types of human prostate strips, including GS≤6, GS = 7, and GS = 8, were divided to evaluate the feasibility of WT-PASA for the aggressiveness of PCa. For the stability of the system, each sample was detected 10 times and all the data thus obtained were used for ResNet-18 classification. The specific sample sizes are listed in Table 1. Thereafter, all the samples were fixed in formalin and sent for pathological examination. Each sample was fixed on glass sides and stained with standard hematoxylin-eosin (HE), Masson trichrome, and Nile red staining.

2.2. Ex vivo PA experiments on human prostate biopsy needle strip

The schematic of the *ex vivo* PA experimental setup is shown in Fig. 2 (a). A tunable optical parametric oscillator (OPO) laser (Phocus Mobile, OPOTEK, Carlsbad, CA) generates the optical illumination with a 10 Hz repetition rate and a 2–5 ns pulse width at a wavelength of 1210 nm (mainly absorbed by lipid molecular) [21,53,54] and 1310 nm (mainly absorbed by collagen molecular) [53,54]. The light was focused using the convex lens and coupled to a fiber diffuser that was developed earlier [24,55], as shown in Fig. 2(a). The signal acquisition system, as shown in Fig. 2(b), includes a needle hydrophone that bandwidth is 1–20 MHz (HNC-1500, ONDA Corp., Sunnyvale, CA) and a fiber optics diffuser. 5 mJ optical energy at 1210 nm and 1310 nm were focused at the coupling end of the fiber optics. The optical fiber diffuser (radius: 300 μm, length: 2 cm) coupling was approximately 70%. Considering the optical output area of the fiber diffuser was approximately 0.377 cm^2, we can determine the optical energy density at the fiber optics diffuser surface was 13.26 mJ/cm^2. The energy was satisfied within the ANSI limit. As shown in Fig. 2(b), the sample was put on the phantom, avoiding the strong scattering of sound signal caused by any hard boundary. Moreover, tweezers were used to make the sample stick close to the optical fiber diffuser, so that it stays straight. In this study, the gel volume was used for coupling the PA signal from the sample. The hydrophone was received in the direction of the extension line of each sample. The PA signals acquired by the hydrophone were received a 35 dB gain by a low-noise amplifier (5072PR, Olympus Corp., Tokyo, Japan). The PA signals received by the hydrophone were recorded by a digital oscilloscope (HDO6000, oscilloscope, Teledyne Lecroy, USA) at a sampling rate of 2500 MHz. A personal computer with LabView was used to control the synchronized laser firing. The typical PA time-domain signal of human prostate biopsy needle strip at both wavelengths are as shown in Fig. 2(c)-(d). The SNR is around 19 dB and 22 dB at 1210 nm and 1310 nm respectively.

2.3. PA signal processing

All PA signal processing was performed using the MATLAB software (Matlab R2018a). In Fig. 3(a), the PA signals generated by each sample was selected with an effective PA signal of approximately 10 μs,

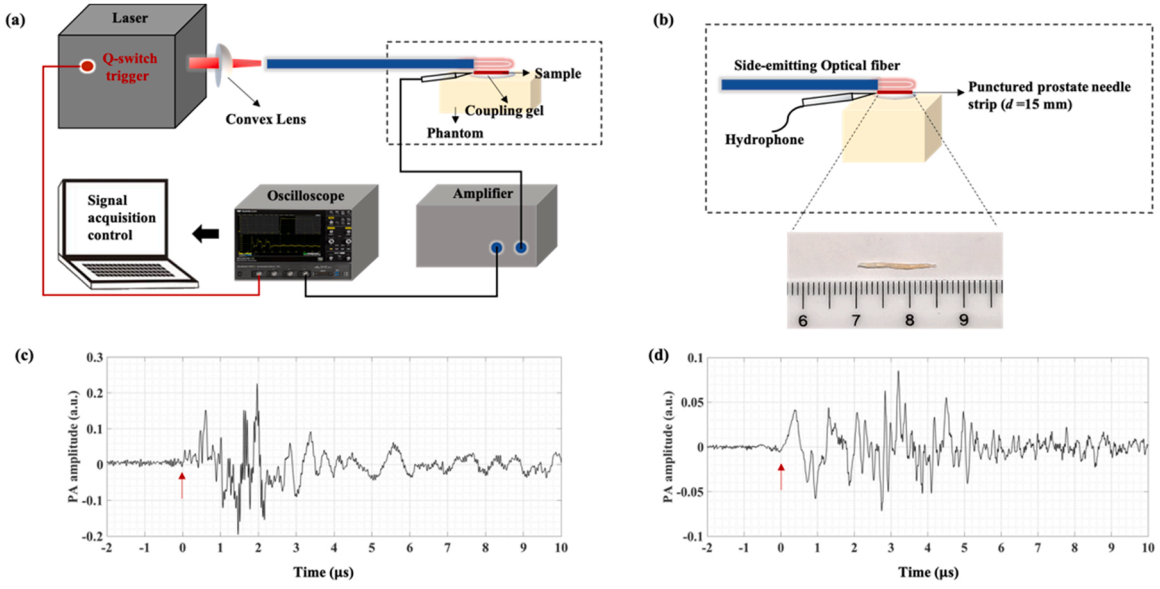

Fig. 2. *Ex vivo* experimental measurement setup. (a) PA measurement setup. (b) PA signal acquisition device. (c) Typical PA time-domain signal of human prostate cancer biopsy needle strip at 1210 nm (Gleason score = 7). (d) Typical PA time-domain signal of human prostate cancer biopsy needle strip at 1310 nm (Gleason score=7). (red arrows in c and d mean the signal start point.). (For interpretation of the references to colour in this figure, the reader is referred to the web version of this article.)

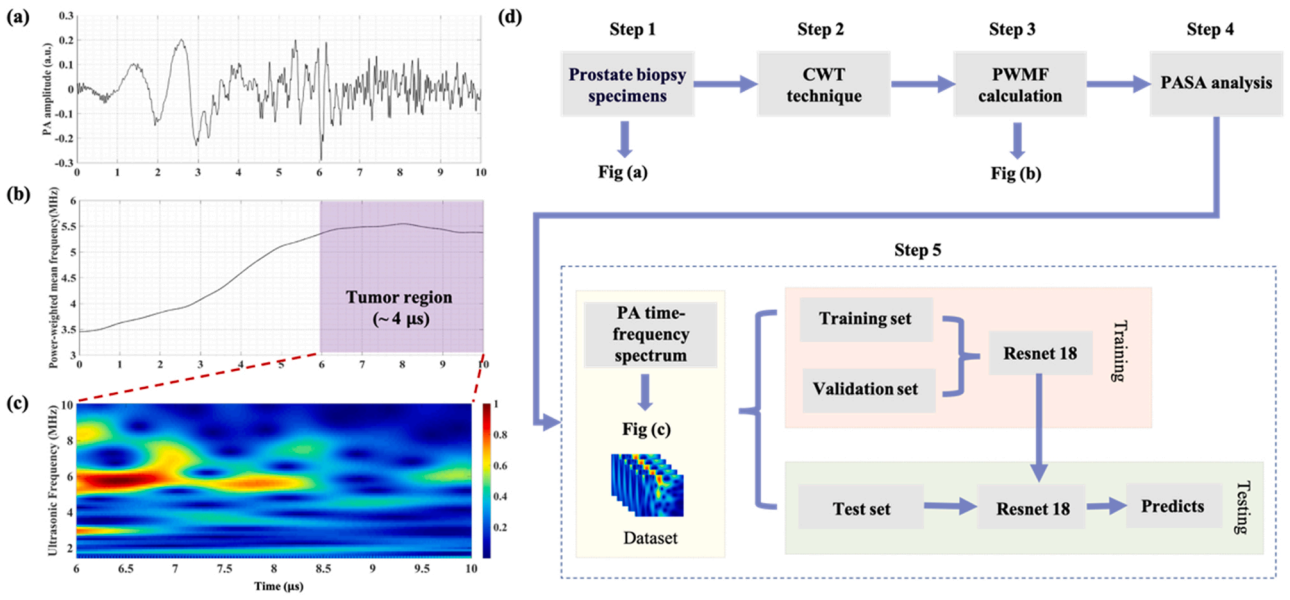

Fig. 3. PA signal processing. (a) Typical PA time-domain signal of human PCa biopsy needle strip. (b) PWMF curve of the effective signal. (c) Corresponding PA time-frequency spectrum (PA-TFS) of the tumor region. (d) The block diagram of the PA signal processing.

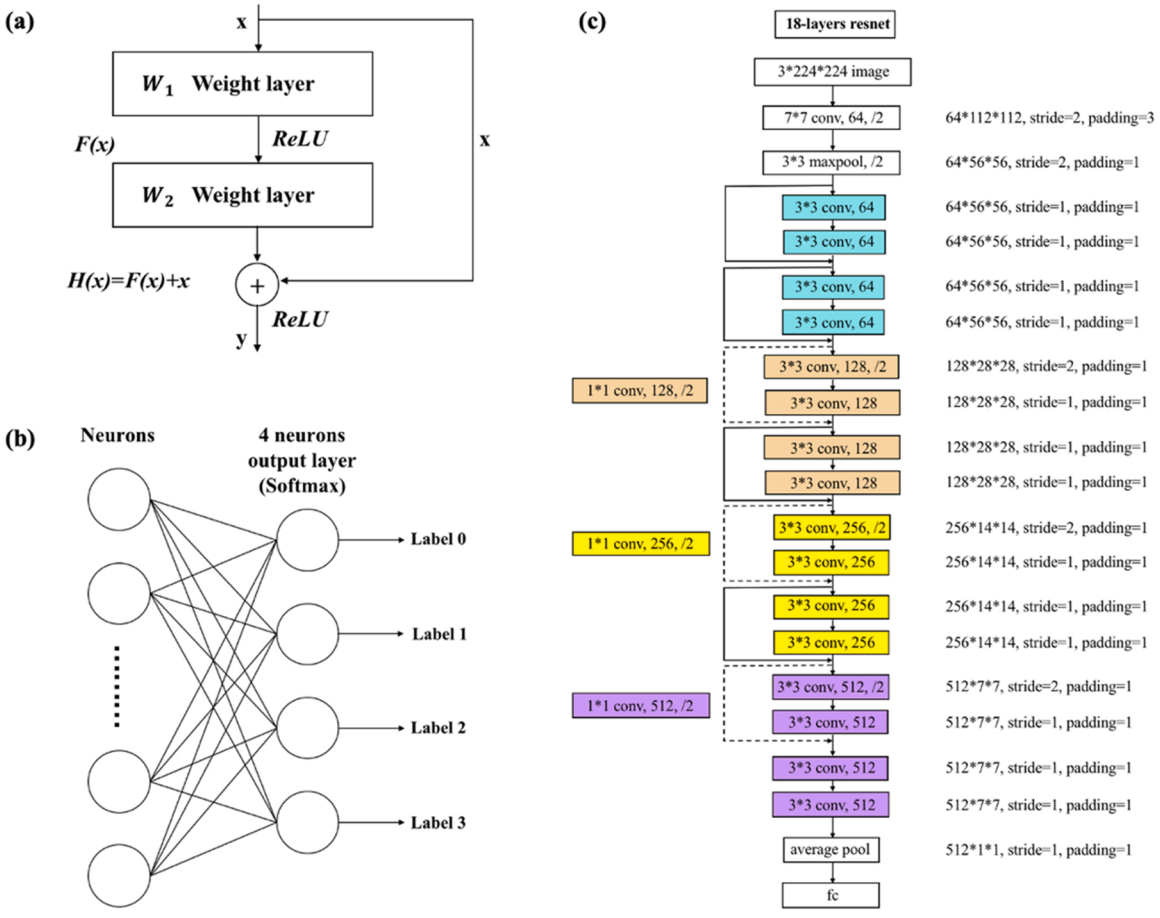

Fig. 4. (a) The residual block (b) The fully connected layers. (c) ResNet-18 architecture.

corresponding to the length of 15 mm with the sound speed of 1500 m/s. Then, the CWT technique was applied to the effective signals (~10 μs) of each prostate strip sample to obtain the PA-TFS depicting the frequency-spectrum distribution at different times. Then, the power-weight mean frequency (PWMF) along the time axis was calculated, which reflects the tissue structural size of the different location of the whole sample. The PWMF was calculated as follows,

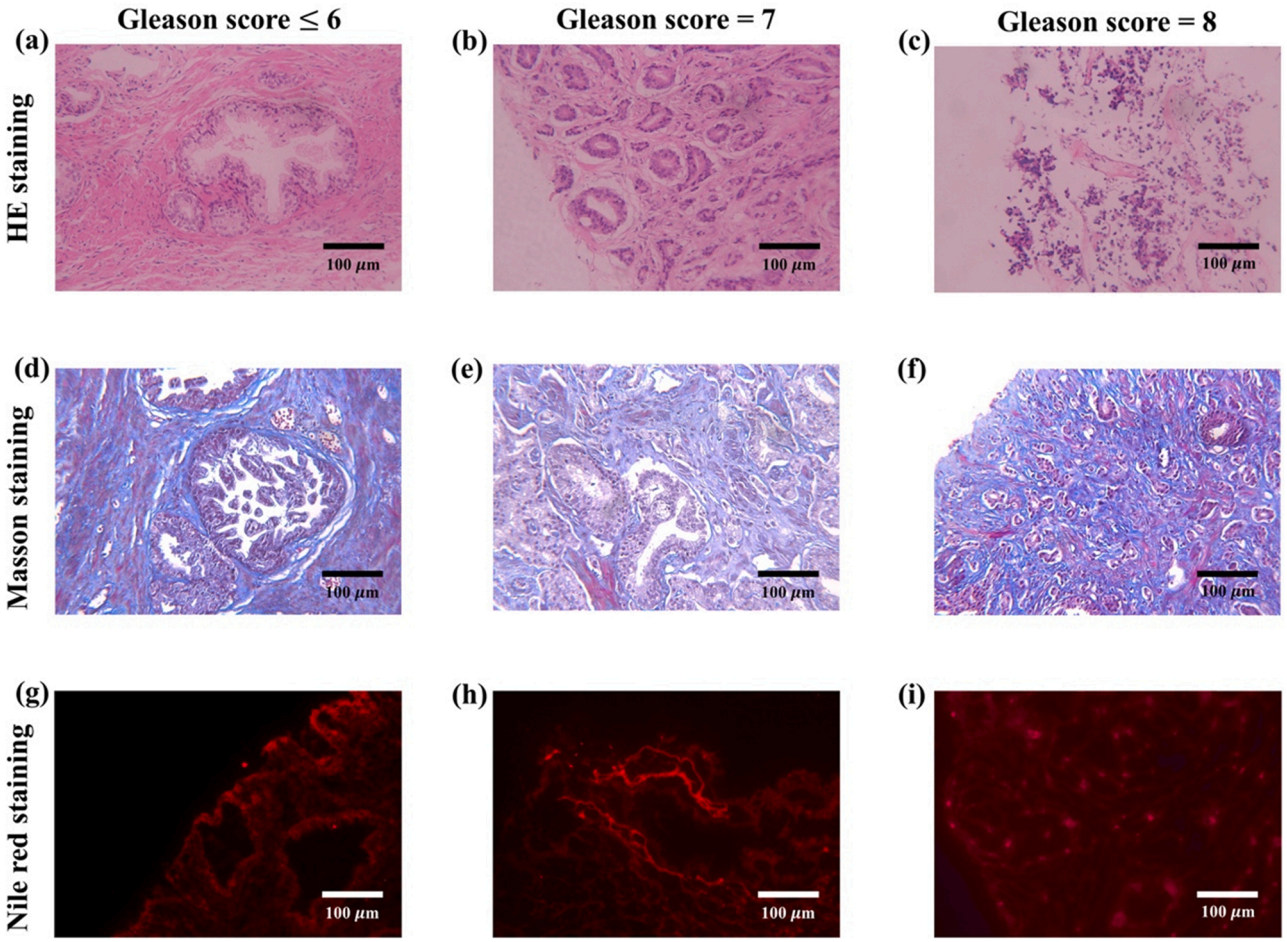

Fig. 5. Representative pathology of (a)-(c) HE staining for different GSs. (d)-(f) Masson staining for different GSs. (g)-(i) Nile red staining for different GSs.

$$PWMF = \frac{\int_{f_1}^{f_2} f \bullet P(f) df}{\int_{f_1}^{f_2} P(f) df} \tag{1}$$

where $P(f)$ represents the spectrum density at frequency f, while f_1 and f_2 are the upper and lower limit of integration. The curve of the PWMF over time is shown in Fig. 3(b). The time axis represents different locations of the whole sample. The PWMF value at each location reflects the average tissue structural size. In general, the poorer the differentiation, the higher Gleason score and the smaller size of glandular cavity structure appears, leading to a higher PWMF value. Because only 20–30% of the whole human prostate biopsy needle strip was tumor region [6–9], we choose the highest value of the PWMF curve as the center, and total 4 μs PA signal length was selected as the tumor region, as shown in the Fig. 3(b). Then we performed PASA only on the tumor region to assess its heterogeneity, excluding the effect of the normal region. A linear fitting of the power spectrum curve was performed to obtain the quantified parameter *slope* to evaluate the heterogeneity of the tumor region. Finally, we further utilized ResNet 18 for intelligent classification of the PA-TFS images of the tumor region, which is shown in Fig. 3(c). The frequency range of 1.5 – 10 MHz was chosen for the PA analysis, considering the feature size of glandular cavity is over 150 μm (<10 MHz) and excluding the low frequency system noise.

Fig. 3(d) is a block diagram of the PA signal processing. In step 1, the PA measurements at each wavelength for each sample was collected. In step 2, CWT technique was applied to the effective signals. In step 3, the PWMF value at each position was calculated, to select the tumor region. In step 4, a linear fitting of the power spectrum curve was performed to obtain the quantified parameter *slope* to evaluate the heterogeneity of the tumor region. In step 5, we further utilized Resnet 18 for intelligent classification of the PA-TFS images of the tumor region. The input data format was ".jpg," and the input image size was "3 × 224 × 244", where 3 is for 3 RGB channels. The color in PA-TFS images represents the intensity information, so RGB data was used as input data, and "224 × 224" was used for the pixel matrix."

2.4. ResNet-18 architecture

We employed ResNet-18 to classify the PA-TFS images of the tumor region directly to obtain more information and grade, and its architecture is shown in Fig. 4. The source code was downloaded from Github with the parameters of was modified to achieve the goal of prostate cancer grading. We modified the parameters of epoch, batchsize, learning rate and the channel number of output and input to achieve the highest accuracy of the four categories at both two wavelengths. The residual block in ResNet18 [56–60] is defined as follows:

$$y = F(x, \{W_i\}) + x \tag{2}$$

where x is the input of the layers and y is the output. $F(x, \{W_i\})$ represents the residual mapping to be learned. There are two weight layers in the residual block [56]; W_1 for the first layer and W_2 for the second layer, as shown in the Fig. 4(a). The residual block can retain the information from the previous layers and resolve the degradation owing to the increase in the number of layers in ResNet. ResNet-18 can retain more of the low-scale features because it is shallow. In this study, as shown in Fig. 4, the ResNet-18 contains 16 convolution layers, 2 downsampling layers, and one fully connected layer (FC). The FC means one fully connected layer. In mathematics, it can be understood as an

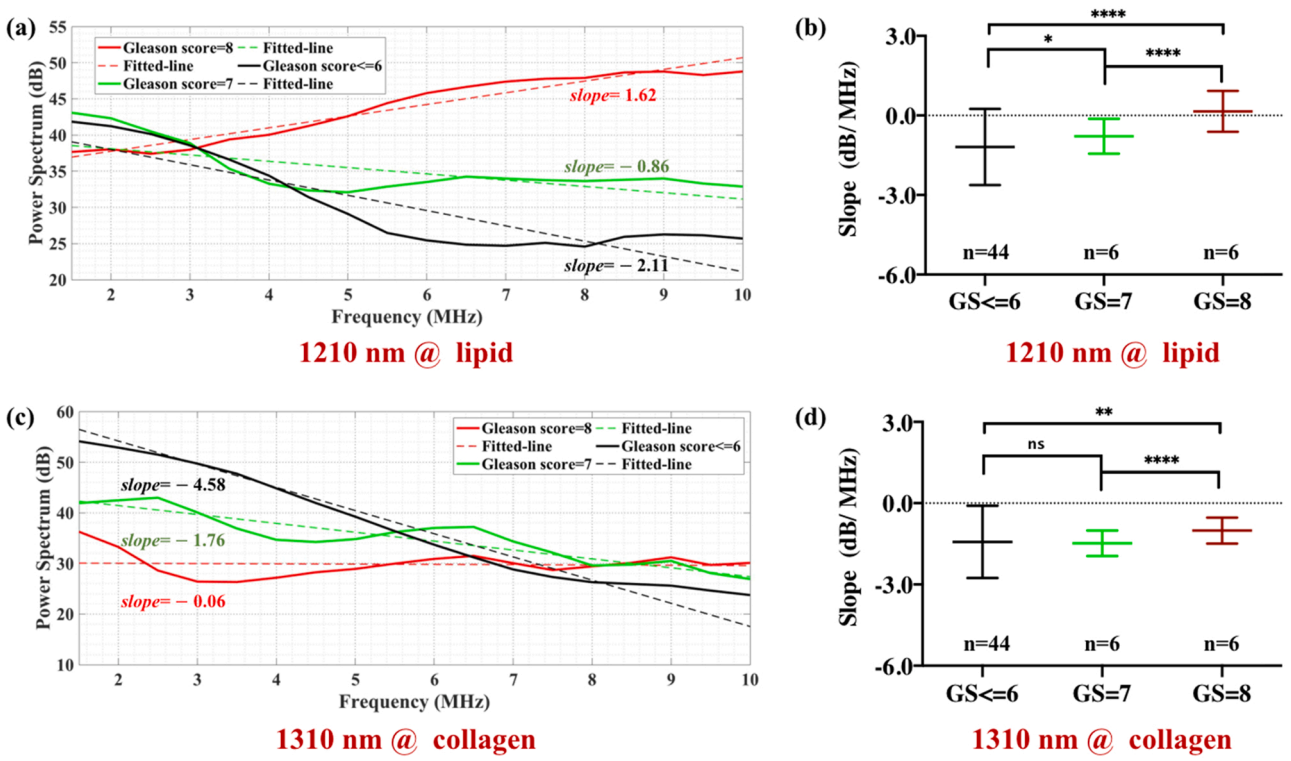

Fig. 6. Results of *ex vivo* PASA of different GS tissues at two wavelength of 1210 nm and 1310 nm. (a) Typical photoacoustic power spectrum analysis (PASA) of different GS (GS≤6, =7, and =8) at the wavelength of 1210 nm. (b) Statistic result of quantified PASA parameters *slope* in different GS at 1210 nm. (c) Representative PASA parameters *slope* of different GS (GS≤6, =7, and =8) at the wavelength of 1310 nm. (d) Statistic result of quantified PASA parameters *slope* in different GS at 1210 nm, n represent the sample size. (**** $p < 0.0001$, ** $p < 0.01$, * $p < 0.1$, ns: not statistically significant.).

Table 2
The number of images in dataset.

Label	Normal 0	GS = 6 1	GS = 7 2	GS = 8 3
Traning setValidation setTest setTotal images	2723434340	801010100	486660	486660

expanded polynomial, as shown in the Fig. 4(b). The size of the convolution kernel in the first convolution layer is 7 × 7, and the rest of the layers are 3 × 3. After average pooling the feature map of the last convolution layer, an eigenvector is obtained by FC, and the classification probability is obtained by normalization with Softmax. Softmax is the node activation function, and it can be defined as:

$$Softmax(z_i) = \frac{e^{z_i}}{\sum_{c=1}^{C} e^{z_c}} \tag{2}$$

where z_i is the output value of the i^{th} node, and C is the number of output nodes. As shown in Fig. 4(c), a residual block is formed by two convolution layers of the same color. In this work, we applied the ResNet-18 model directly on the PA-TFS images of the tumor region to obtain more information, and then eventually grade the GS. A total of 560 images were used for training ResNet-18. Among these images, 448 (80%), 56 (10%), and 56 (10%) were used for network training, validation, and testing, respectively. [We implement our experiments on PyTorch, using an Intel Xeon Gold 6130 CPU and a Nvidia Quadro P4000 GPU. The training is run with Adam for 100 epochs, with a learning rate of 0.001 and batch size of 16.].

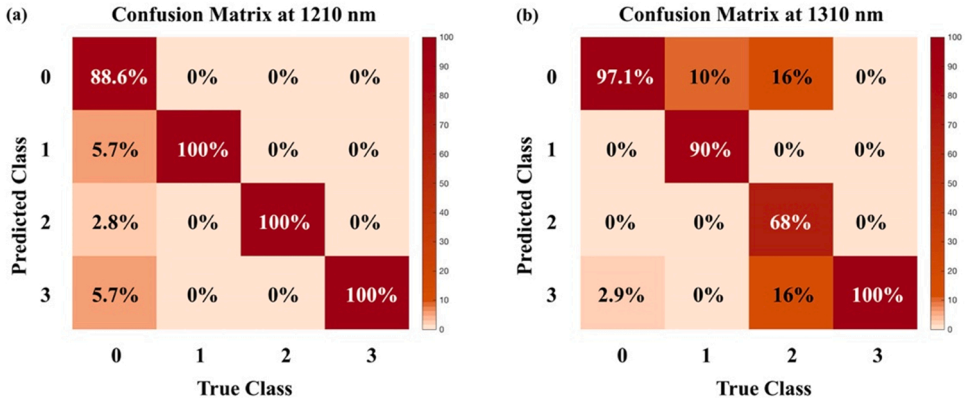

Fig. 7. ResNet-18 network classification results of different GSs at 1210 nm and 1310 nm. (a) Confusion matrix of normal and different GSs (GS = 6, 7 and 8) tissues at 1210 nm (total accuracy of 89.3%). (b) Confusion matrix of normal and different GSs (GS = 6, 7 and 8) tissues at 1310 nm (total accuracy of 92.7%).

3. Results

3.1. Pathological results

Normally, collagens are the structural network supporting prostate tissues [61,62], while lipids are exist in exosomes of the extracellular environment [63]. They are mainly distributed around the glandular cavity. However, when prostate tissues are cancerous, the environment changes and metabolism is abnormal [64], which leads to the change of structure. Therefore, lipids and collagens are especially evident owing to the microstructural changes of these two biological macromolecules during the development of prostate cancer. In this study, we observed the correlation of photoacoustic spectrum and prostate cancer at 1210 nm and 1310 nm. The pathological results of standard HE staining, Masson staining, and Nile red staining are shown in Fig. 5. HE staining in Fig. 5(a)-(c) shows that the degree of tissue differentiation decreases with the increase in GS. GS≤6 has the highest differentiation and a relatively complete glandular cavity structure. With the increase in GS, the tissue gradually changed from highly differentiated to poorly differentiated, as shown in Fig. 5(b), with the appearance of smaller glandular cavity structures. For GS = 8 with the lowest differentiation, there was no complete glandular cavity structure, and the cell was diffused in the tissue. In general, the poorer the differentiation, the smaller size of glandular cavity structure appear. We also conducted Masson staining and Nile red staining to further discuss the changes in the structure of lipid and collagen molecules with increased GS. As shown in Fig. 5(d)-(f), we can observe that the collagen molecules are distributed around the glandular cavity, showing that the structural changes of collagen molecules are similar to the changes in glandular cavity structures. The same conclusion can be obtained for lipid molecules from Fig. 5(g)-(i). Resolvable microscopic features (>150 μm) were formed by the glandular cavity (surrounded by lipid and collagen molecules).

3.2. Quantified PASA parameters slope of different GS tissues

Four types of human PCa needle strips, including benign (34 samples), GS = 6 (10 samples), GS = 7 (6 samples), and GS = 8 (6 samples), were collected for this study. The PASA *slope* indicates the relative proportion between the high- and low-frequency components in the tumor region. As shown in Fig. 6(a), with a higher GS, a higher frequency appears, leading to a higher *slope*. Thus, the higher the *slope*, the smaller the size of the glandular cavity and the higher the heterogeneity. As shown in Fig. 6(c), there is a lower *slope* for the lower GS. To make the result more intuitive, the statistical result of the *slope* at 1210 nm and 1310 nm were calculated. As shown in Fig. 6(b), the *slope* increased significantly when GS = 8 as compared to when GS≤6 ($p < 0.0001$) and GS= 7 ($p < 0.0001$). At the collagen absorption wavelength of 1310 nm, the *slopes* were higher when GS = 8 as compared to when GS = 7 and GS = 6, as shown in Fig. 6(d). Owing to the limited sample size, only statistical analysis could be conducted to obtain qualitative results. The aforementioned results were consistent with the three pathological staining results presented in Fig. 5(d)-(i).

3.3. Classification results of using ResNet-18 network

Further, we employed the ResNet-18 network to obtain more information on the PA to quantify different GSs in detailed. We labeled four groups of normal, GS= 6, GS= 7, and GS= 8 with 0, 1, 2 and 3. A total of 560 images were used for ResNet-18 network. We labled all the images according to the pathological results of Gleason score. There were 340 images of normal tissues, 100 images of GS= 6 tissues, 60 images of GS= 7 tissues, and 60 images of GS= 8 tissues. In this study, the training, validation and test sets were divided in a ratio of 8:1:1, the number of images in dataset is shown in Table 2. The total accuracy was 89.3% at 1210 nm and 92.7% at 1310 nm. As shown in Fig. 7(a), all the four groups achieved reasonably high precisions of 88.6%, 100%, 100%, and 100% on normal, GS = 6, GS = 7 and GS= 8, respectively, at 1210 nm. As shown in Fig. 7(b), all four groups also achieved reasonably high precisions of 97.1%, 90%, 68%, and 100% on normal, GS = 6, GS = 7 and GS= 8, respectively, at 1310 nm. The common misclassification of groups is observed between "normal" and "GS= 6" or "GS = 7' and "GS = 8", as shown in Fig. 7(b), because of the small sample size of GS= 7 and similar structural characteristics between adjacent GS scores. As shown in Fig. 7(b), it seems there was a small percentage of normal tissues misclassified as highest grade rather than lower ones. Because of the limit sizes of GS= 8 tissues, leading to the incomplete extraction of feature information.

4. Discussion

PASA is widely used in disease detection [22,23,26–30] because of its ability to accurately quantify molecular physicochemical information difference. However, because the human prostate biopsy needle strips are different from other disease models, the tumor region is usually less than half of its total length. The PA signals were generated from both normal tissue and tumor tissue, leading to the *slope* of PASA parameter reflecting the averaged microstructure characteristics of the whole sample, rather than the microstructure characteristics of tumor tissue. In this work, we combined CWT technique with PASA to accurately quantify the structural changes only in tumor region. First, CWT was applied to the effective signals (~10 μs) of each sample to obtain PA-TFS depicting the frequency-spectrum distribution at different times. Then, PWMF along the time axis was calculated, which reflects the tissue structural size of the different location of the whole human prostate biopsy needle strip. In general, the poorer the differentiation, the higher the Gleason score and the smaller size of glandular cavity structure that appears, leading to a higher PWMF value. Because only 20–30% of the whole human prostate biopsy needle strip was the tumor region [6–9], we chose the highest value of the PWMF curve as the center, and total 4 μs PA time-domain signal length was selected as the tumor region. The PA signal acquisition device was fabricated by a home-made fiber optics diffuser [24,55] and a needle hydrophone and the hydrophone received in the direction of the extension line of each sample. We extracted the parameter of PWMF to distinguish tumor region from the whole human prostate strips. The amplitude of the frequency components in the power spectrum was calculated as the weighted coefficient, and we can obtain the main frequency of the whole human prostate strips by PWMF. We only conducted PASA on the tumor region and quantified the aggressiveness of PCa using the PA parameter of the *slope*. The higher the GS, the larger the *slope*. The aforementioned results were consistent with the three pathological staining results presented in Fig. 5(d)-(i). The results also indicate that PASA was able to successfully distinguish high-risk tumors (GS≥7) from the lower-risk ones (GS≤6). PASA is therefore a highly objective, quantitative, and accurate grading approach. As we distinguished different GS prostate tissues through the change in the structural size, because of individual differences, the degree of differentiation may not significantly vary between the lower GS (GS≤6 and GS=7), as shown in Fig. 6(d). The extraction of one parameter of *slope* may not provide a clear distinction. Because the sample size is limited, only statistical results can be used for quantitative analysis, and the method is not suitable for grading an individual currently. ResNet-18 is used to acquire more PA information and grade different GS tissues in detail. Deep learning extracts more PA information to achieve better classification, for example the information of the PA intensity at different locations and frequencies, the overall accuracy rate for the distinction between the four different tissues was greater than 89%, as shown in Fig. 7(a) and (b).

The feasibility of grading PCa tissue with different GS using the WT-PASA method was demonstrated in this study. The PA parameter extracted in this study was relatively simple and only covered the structural size. In the future, we will attempt to extract more

dimensional parameters to comprehensively evaluate the physical properties of tissues, such as the curvature of the cavity and elasticity. More samples should be accumulated and additional data should be used in the ResNet-18 to improve the accuracy of the tissues with high GS. In fact, the accuracy rate gradually increased with the continuous accumulation of the sample size during the last two years. Furthermore, thus HE staining is the result of staining the nucleus, and the PA absorption band of the nucleus falls in the ultraviolet (UV) wavelengths band [23]. As the result, we intend to include ultraviolet (UV) wavelengths to quantify the GS and then directly compare it with the H&E stained histology results to acquire additional comprehensive diagnostic information.

5. Conclusion

WT-PASA method can be used to comprehensively and accurately distinguish the influence of the GS structure size on the tumor region based on the PWMF difference to eliminate the influence of normal tissue on PASA parameters in the prostate section. From the pathological results, we were able to identify that the lipid and collagen molecules grow around the glandular cavity structure. Further, the *slope* was found to be related to the size of the glandular cavity structure and can be used for grading GS: a high GS indicated a small glandular cavity structure and a high *slope*. In addition, we used ResNet-18 to comprehensively classify different GSs, with an accuracy of more than 89% at both 1210 nm and 1310 nm wavelengths. The PA results were consistent with the pathological results, demonstrating that the proposed approach can objectively and effectively assess the aggressiveness of PCa. In addition, for each sample, the PA detection time was about 3 min. The post-processing time was approximately 2 min, and decision-making time about 1 min. All the procedure done took less than 7 min, which was about the same for all samples. In the future, we aim to miniaturize and integrate the PA signal acquisition device into a fine needle, thereby achieving minimal invasive assessment of the aggressiveness of PCa in vivo and relieving patients' pain and complications such as inflammation caused by needle biopsies.

Ethical approval

All procedures performed in studies involving human participants were in accordance with the ethical standards of the institutional and/or national research committee and with the 1964 Helsinki declaration and its later amendments or comparable ethical standards.

Declaration of Competing Interest

The authors declare that they have no known competing financial interests or personal relationships that could have appeared to influence the work reported in this paper.

Acknowledgement

This work was supported by the National Natural Science Foundation of China (no. 12034015 & 81702962), Clinical Research Plan of SHDC (no. SHDC2020CR3074B) Program of Shanghai Academic Research Leader (21XD1403600) and Shanghai Municipal Commission of Science and Technology Project (19511132101). We would like to thank Editage (www.editage.cn) for English language editing.

Appendix A. : Simulation work

To evaluate the feasibility of the WT-PASA method, we implemented numerical simulation on a model with the modified Gleason grading diagram in advance, as shown in Fig. A1. We extracted the three typical groups (GS≤6, GS = 4 +3 = 7, GS = 8) that affect the PA power spectrum for the simulation and simplified the model to a two-dimensional entity without loss of physical meaning. The simulated model was scaled to the actual human PCa biopsy needle strip size. The total length of the simulated model was scaled to 15 mm. The length of the simulated GS≤6, GS= 3 + 4 = 7 and GS= 8 model was scaled to 5 mm respectively. The software used for PA simulation was the MATLAB k-wave toolbox (R2019b, MathWorks, Natick, MA) [52]. According to the simulation setting in k-wave, the white pixels in Fig. A1(a) represent the microstructure of human PCa biopsy needle strip, and they were designated as PA sources with the initial acoustic pressure of 1, whereas the black pixels were designated as the other biological tissue without initial acoustic pressure. The speed of sound was set at 1500 m/s for the simulated area, and an acoustic sensor was placed on the extension line along the length direction of the simulated model to receive PA signals, as shown in Fig. A1(b). The distance of the acoustic sensor to the simulated model was set to 3 mm. Fig. A1(c) shows typical PA signals of the simulated model.

Fig. A2(a) shows the PA-TFS image of the simulated model with three typical Gleason groups (GS≤6, GS=4 +3 =7 and GS=8). The PA-TFS images reflect the frequency spectrum distribution at each moment, reflecting different levels of malignancy corresponding to different location. In the region of GS≤6, as shown in Fig. A2(a), there are lower frequencies than GS= 4 + 3 = 7 and GS= 8 regions. By contrast, much higher frequencies appeared in the GS= 8 regions. The reason for this is that the poorer the differentiation, accompanied by the smaller size of glandular cavity structure appearing. It is consistent with the theory that PA signals produced from smaller size structures have higher acoustic frequency components [25–28]. To choose the region with the highest degree of malignancy, we propose the parameter PWMF. We calculate PWMF along the time axis and propose an average PWMF for each group to characterize its structure, as shown in Fig. A2(b). We can see GS= 8 group has higher average PWMF, and PWMF can help choose the region with the highest degree of malignancy. Then, we conduct PASA on each group, proposing the parameter *slope* to grade GS. As shown

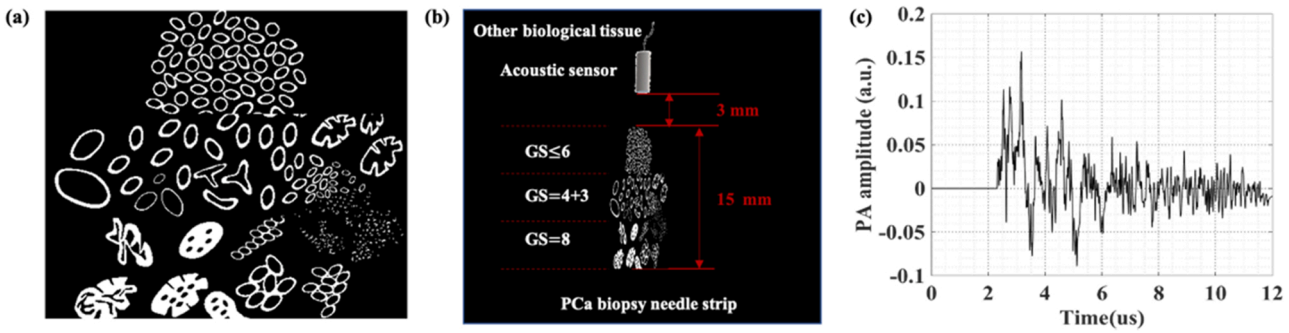

Fig. A1. (a) Simulation model. (b) Simulation area setting. (c) Simulated photoacoustic signal in time domain.

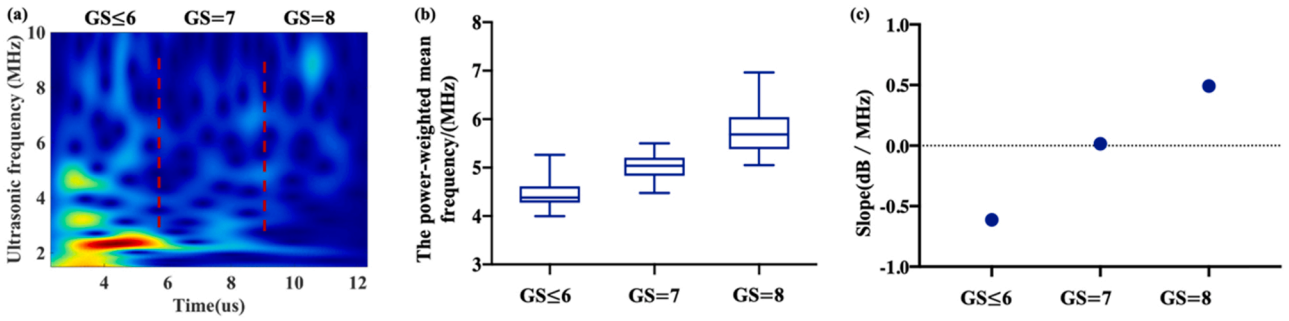

Fig. A2. Results of numerical simulation. (a) Photoacoustic time-frequency spectrum (PA-TFS) of the simulated model. (b) The average power-weighted mean frequency (PWMF) of three groups (GS≤6, GS=7 and GS=8). (c) Photoacoustic power spectrum analysis (PASA) parameters *slope* of different GS (GS≤6, =7, and =8).

in Fig. A2(c), GS= 8 group has higher *slope*, which is consistent with the result of the appeared higher frequency and disappeared lower frequency in Fig. A2 (a).

Appendix B. : Power study to determine the number of patients needed

Before we performed the dual-wavelength photoacoustic detection experiment before, we performed the photoacoustic detection based on the punctured prostate tissue strips (including 3 groups). Moreover, we performed power studies using PASS software to calculate the minimum number of samples required in experiment. In particular, three-sample (GS≤6, GS=7 and GS=8) F-test assuming equal variance were prepared. The results are shown as follows:

- Based on the results at 1210 nm, the mean values of *slopes* were − 1.16 (GS≤6), − 0.66 (GS=7) and 0.5 (GS=8) respectively, and the numeric results for three-sample F-test assuming equal variance are shown in Table B1 and Fig. B1.

Table B1
Power study results based on *slopes* of photoacoustic power spectrum at 1210 nm.

Target power	Actual power	Average n	G (group)	Total N	K (means multiplier)	Std Dev of σm	Standard Deviation σ	Effect Size	Alpha
0.7	0.7866	6	3	18	1	0.67	0.66	1.0194	0.01
0.8	0.8828	7	3	21	1	0.67	0.66	1.0194	0.01
0.9	0.9393	8	3	24	1	0.67	0.66	1.0194	0.01
0.7	0.76	4	3	12	1	0.67	0.66	1.0194	0.05
0.8	0.8825	5	3	15	1	0.67	0.66	1.0194	0.05
0.9	0.9461	6	3	18	1	0.67	0.66	1.0194	0.05

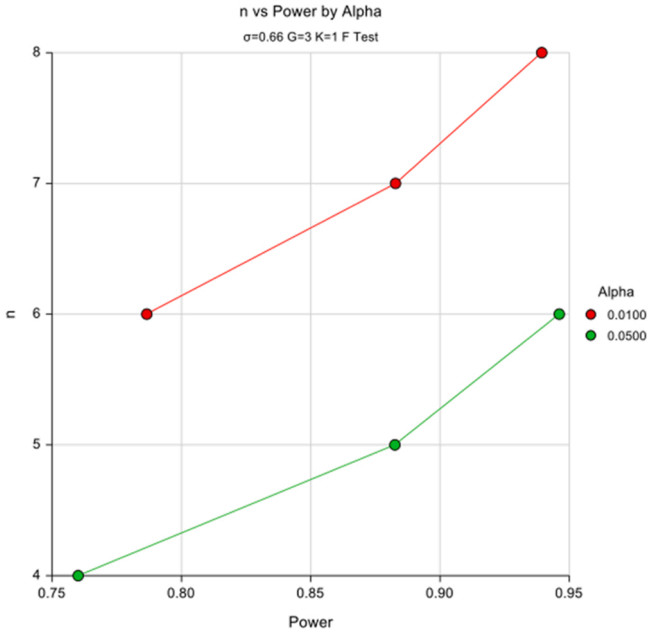

Fig. B1. Power study results based on slopes of photoacoustic power spectrum at 1210 nm.

- Based on the results at 1310 nm, the mean values of *slopes* were − 1.83 (GS≤6), − 1.48 (GS=7) and − 1.01 (GS=8), respectively, and the numeric results for three-sample F-test assuming equal variance are shown in Table B2 and Fig. B2.

Table B2
Power study results based on *slopes* of photoacoustic power spectrum at 1310 nm.

Target power	Actual power	Average n	G (group)	Total N	K (means multiplier)	Std Dev of σm	Standard Deviation σ	Effect Size	Alpha
0.7	0.7847	8	3	24	1	0.34	0.4	0.8399	0.01
0.8	0.8556	9	3	27	1	0.34	0.4	0.8399	0.01
0.9	0.9059	10	3	30	1	0.34	0.4	0.8399	0.01
0.7	0.7273	5	3	15	1	0.34	0.4	0.8399	0.05
0.8	0.8281	6	3	18	1	0.34	0.4	0.8399	0.05
0.9	0.938	8	3	24	1	0.34	0.4	0.8399	0.05

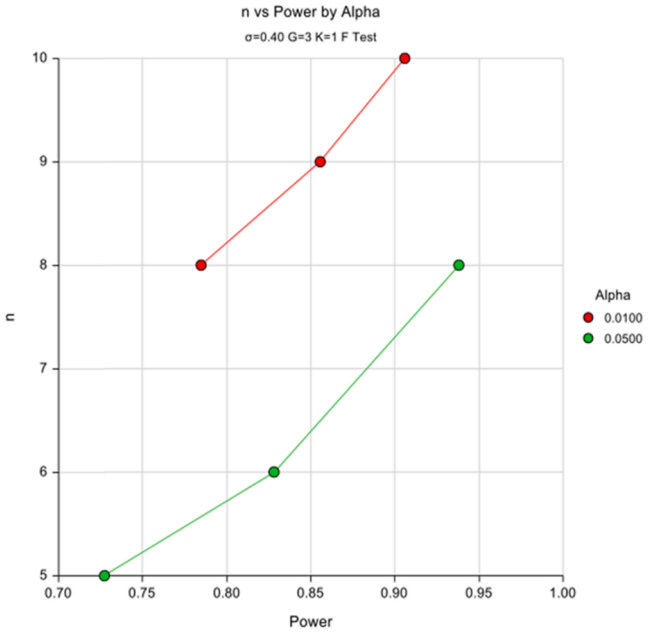

Fig. B2. Power study results based on slopes of photoacoustic power spectrum at 1310 nm.

According to the power study results, each group sample size from 5 to 10 can meet the minimum sample requirements. Thus, over the last two years, we collected totally 56 punctured prostate tissue strip samples (34 for normal tissue, 10 for GS=6 tissue, 6 for GS=7 tissue and 6 for GS=8 tissue). For the stability of the system, each sample was detected 10 times and all the data thus obtained were used for ResNet-18 classification (total 56 samples for WT-PASA analysis and 560 images for ResNet-18 classification). All participants provided their informed consent, and all procedures were approved by the Institutional Review Committee of Tongji Hospital.

Appendix C. : Photoacoustic experimental results

Figs. C1 and C2 show the typical PA time-domain signals, corresponding PWMF curve and PA-TFS of the tumor region of different GS samples at 1210 nm and 1310 nm, respectively.

As shown in Fig. C1(b), (e), (h) and C2(b), (e), (h), the power-weight mean frequency (PWMF) along the time axis is different, which reflects the difference of tissue structural size at different location. With higher malignant degree, the smaller size of glandular cavity structure appearing, which lead to PA signals have higher acoustic frequency components [25–28]. As shown in Fig. C1(a), (d), (g) and C2(a), (d), (g), PA time-domain signals having highest acoustic frequency components corresponds to the highest PWMF value. It shows that PWMF can help us choose the tumor region. Further, we can see PWMF also can qualitatively reflect the GS grade, it shows that GS= 8 tissues with highest PWMF value and GS≤ 6 with the lowest at both two wavelengths. As shown in Fig. C1(c), (f), (i) and C2(c), (f), (i), we can see that PA time-frequency spectrum (PA-TFS) of the highest-grade tissues (GS=8) have much higher acoustic frequency than others, and PA-TFS were totally different between different GS tissues, which can be the characteristic parameter for machine learning.

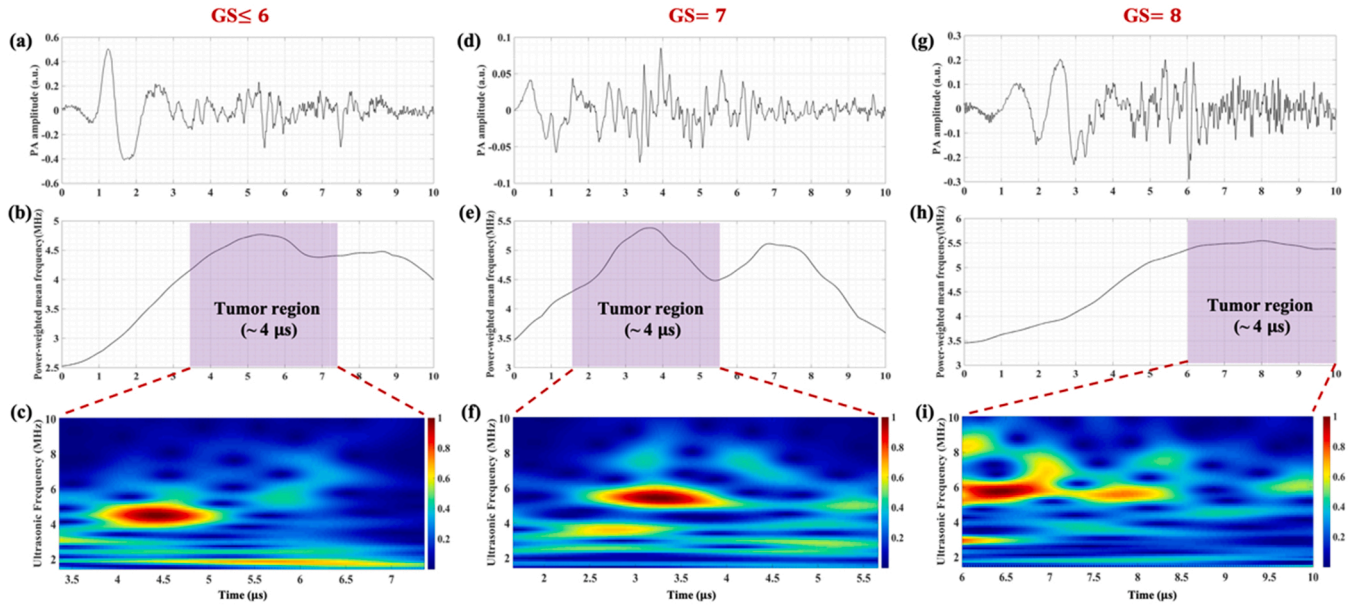

Fig. C1. Photoacoustic detection results at 1210 nm (a), (d), (g) Typical PA time-domain signal of human prostate cancer biopsy needle strip (Gleason score(GS)≤6, GS= 7 and GS= 8). (b), (e), (h) Corresponding PWMF curve of the effective signal. (c), (f), (i) Corresponding PA time-frequency spectrum (PA-TFS) of the tumor region.

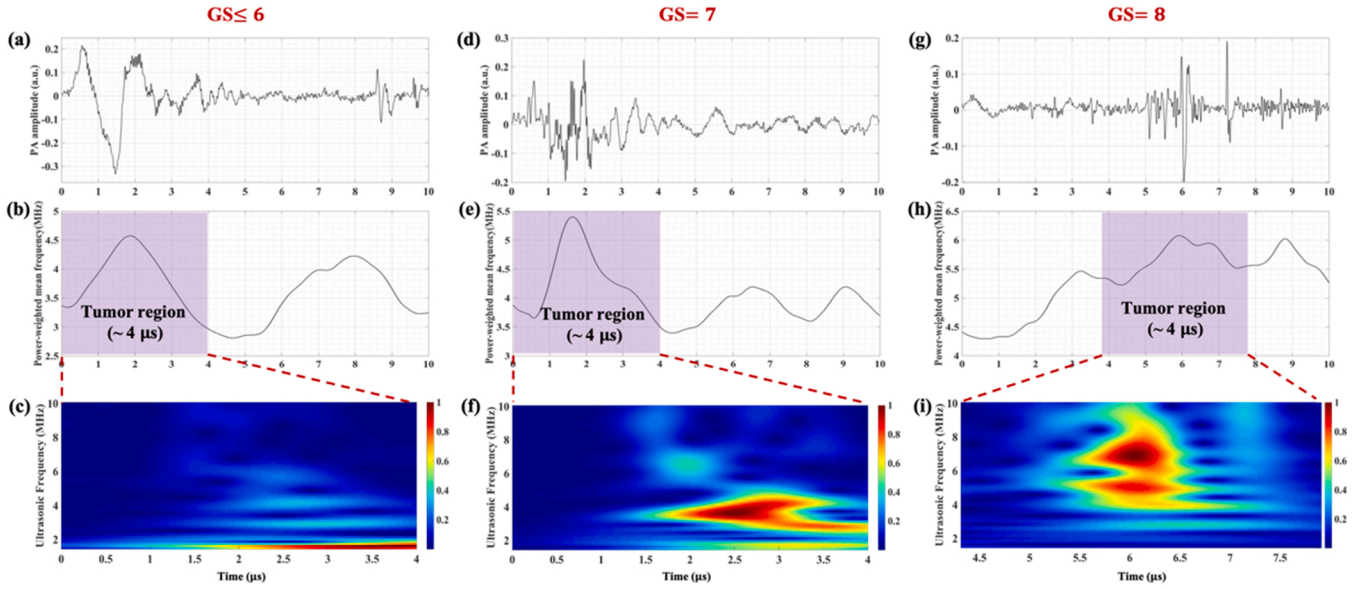

Fig. C2. Photoacoustic detection results at 1310 nm (a), (d), (g) Typical PA time-domain signal of human prostate cancer biopsy needle strip (Gleason score(GS)≤6, GS= 7 and GS= 8). (b), (e), (h) Corresponding PWMF curve of the effective signal. (c), (f), (i) Corresponding PA time-frequency spectrum (PA-TFS) of the tumor region.

References

[1] J.M. Fitzpatrick, C. Schulman, A.R. Zlotta, F.H. Schröder, Prostate cancer: a serious disease suitable for prevention, BJU Int. 103 (2009) 864–870, https://doi.org/10.1111/j.1464-410X.2008.08206.x.

[2] J. Ferlay, P. Autier, M. Boniol, M. Heanue, M. Colombet, P. Boyle, Estimates of the cancer incidence and mortality in Europe in 2006, Ann. Oncol. 18 (2007) 581–592, https://doi.org/10.1093/annonc/mdl498.

[3] R.L. Siegel, K.D. Miller, A. Jemal, Cancer statistics, 2018: cancer Statistics, 2018, CA A Cancer J. Clin. 68 (2018) 7–30, https://doi.org/10.3322/caac.21442.

[4] L.C. Harlan, A. Potosky, F.D. Gilliland, R. Hoffman, P.C. Albertsen, A.S. Hamilton, J.W. Eley, J.L. Stanford, R.A. Stephenson, Factors associated with initial therapy for clinically localized prostate cancer: prostate cancer outcomes study, JNCI J. Natl. Cancer Inst. 93 (2001) 1864–1871, https://doi.org/10.1093/jnci/93.24.1864.

[5] N.E. Fleshner, M.S. Cookson, S.M. Soloway, W.R. Fair, Repeat transrectal ultrasound-guided prostate biopsy: a strategy to improve the reliability of needle biopsy grading in patients with well-differentiated prostate cancer, Urology 52 (1998) 659–662, https://doi.org/10.1016/S0090-4295(98)00226-X.

[6] J. Raja, N. Ramachandran, G. Munneke, U. Patel, Current status of transrectal ultrasound-guided prostate biopsy in the diagnosis of prostate cancer, Clin. Radiol. 61 (2006) 142–153, https://doi.org/10.1016/j.crad.2005.10.002.

[7] N.E. Fleshner, M. O'Sullivan, W.R. Fair, Prevalence and predictors of a positive repeat transrectal ultrasound guided needle biopsy of the prostate, J. Urol. 158 (2) (1997) 505–509, https://doi.org/10.1016/S0022-5347(01)64518-X.

[8] J.R. Stark, S. Perner, M.J. Stampfer, J.A. Sinnott, S. Finn, A.S. Eisenstein, J. Ma, M. Fiorentino, T. Kurth, M. Loda, E.L. Giovannucci, M.A. Rubin, L.A. Mucci, Gleason Score and Lethal Prostate Cancer: Does 3 + 4 = 4 + 3? JCO 27 (2009) 3459–3464, https://doi.org/10.1200/JCO.2008.20.4669.

[9] Donald F. Gleason, Histologic grading of prostate cancer: a perspective, Hum. Pathol. 23 (3) (1992) 273–279, https://doi.org/10.1016/0046-8177(92)90108-F.

[10] A.V. Taira, G.S. Merrick, R.W. Galbreath, H. Andreini, W. Taubenslag, R. Curtis, W. M. Butler, E. Adamovich, K.E. Wallner, Performance of transperineal template-guided mapping biopsy in detecting prostate cancer in the initial and repeat biopsy setting, Prostate Cancer Prostatic Dis. 13 (2010) 71–77, https://doi.org/10.1038/pcan.2009.42.

[11] G.S. Merrick, S. Gutman, H. Andreini, W. Taubenslag, D.L. Lindert, R. Curtis, E. Adamovich, R. Anderson, Z. Allen, W. Butler, K. Wallner, Prostate cancer distribution in patients diagnosed by transperineal template-guided saturation biopsy, Eur. Urol. 52 (3) (2007) 715–724, https://doi.org/10.1016/j.brachy.2007.02.085.

[12] G. Fiard, N. Hohn, J.L. Descotes, J.J. Rambeaud, J. Troccaz, J.A. Long, Targeted MRI-guided prostate biopsies for the detection of prostate cancer: initial clinical experience with real-time 3-dimensional transrectal ultrasound guidance and magnetic resonance/transrectal ultrasound image fusion, Urology 81 (6) (2013) 1372–1378.

[13] B. Ehdaie, S.F. Shariat, Magnetic resonance imaging–targeted prostate biopsy: back to the future, Eur. Urol. 63 (2013) 141–142, https://doi.org/10.1016/j.eururo.2012.06.049.

[14] C.M. Moore, N.L. Robertson, N. Arsanious, T. Middleton, A. Villers, L. Klotz, S. S. Taneja, M. Emberton, Image-guided prostate biopsy using magnetic resonance imaging–derived targets: a systematic review, Eur. Urol. 63 (2013) 125–140, https://doi.org/10.1016/j.eururo.2012.06.004.

[15] M.M. Siddiqui, S. Rais-Bahrami, H. Truong, L. Stamatakis, S. Vourganti, J. Nix, A. N. Hoang, A. Walton-Diaz, B. Shuch, M. Weintraub, J. Kruecker, H. Amalou, B. Turkbey, M.J. Merino, P.L. Choyke, B.J. Wood, P.A. Pinto, Magnetic resonance imaging/ultrasound–fusion biopsy significantly upgrades prostate cancer versus systematic 12-core transrectal ultrasound biopsy, Eur. Urol. 64 (5) (2013) 713–719, https://doi.org/10.1016/j.eururo.2013.05.059.

[16] X. Wang, Y. Pang, G. Ku, X. Xie, G. Stoica, L.V. Wang, Noninvasive laser-induced photoacoustic tomography for structural and functional in vivo imaging of the brain, Nat. Biotechnol. 21 (2003) 803–806, https://doi.org/10.1038/nbt839.

[17] L.V. Wang, Photoacoustic Imaging and Spectroscopy, CRC Press, 2009.

[18] L.V. Wang, S. Hu, Photoacoustic tomography: in vivo imaging from organelles to organs, Science 335 (2012) 1458–1462, https://doi.org/10.1126/science.1216210.

[19] G. Xu, J.B. Fowlkes, C. Tao, X. Liu, X. Wang, Photoacoustic spectrum analysis for microstructure characterization in biological tissue: analytical model, Ultrasound Med. Biol. 41 (2015) 1473–1480, https://doi.org/10.1016/j.ultrasmedbio.2015.01.010.

[20] M.P. Patterson, C.B. Riley, M.C. Kolios, W.M. Whelan, Optoacoustic characterization of prostate cancer in an in vivo transgenic murine model, J. Biomed. Opt. 19 (2014), 056008, https://doi.org/10.1117/1.JBO.19.5.056008.

[21] G. Xu, Z.-X. Meng, J.D. Lin, J. Yuan, P.L. Carson, B. Joshi, X. Wang, The functional pitch of an organ: quantification of tissue texture with photoacoustic spectrum analysis, Radiology 271 (2014) 248–254, https://doi.org/10.1148/radiol.13130777.

[22] R.E. Kumon, C.X. Deng, X. Wang, Frequency-domain analysis of photoacoustic imaging data from prostate adenocarcinoma tumors in a murine model, Ultrasound Med. Biol. 37 (2011) 834–839, https://doi.org/10.1016/j.ultrasmedbio.2011.01.012.

[23] G. Xu, M.C. Davis, J. Siddiqui, S.A. Tomlins, S. Huang, L.P. Kunju, J.T. Wei, X. Wang, Quantifying gleason scores with photoacoustic spectral analysis: feasibility study with human tissues, Biomed. Opt. Express 6 (2015) 4781–4789, https://doi.org/10.1364/BOE.6.004781.

[24] H. Zhang, W. Chao, Q. Cheng, S. Huang, X. Wang, D. Wu, G. Xu, Interstitial photoacoustic spectral analysis: instrumentation and validation, Biomed. Opt. Express 8 (2017) 1689–1697, https://doi.org/10.1364/BOE.8.001689.

[25] M. Zhang, Y. Chen, W. Xie, S. Wu, J. Liao, Q. Cheng, Photoacoustic power azimuth spectrum for microvascular evaluation, Photoacoustics 22 (2021), 100260, https://doi.org/10.1016/j.pacs.2021.100260.

[26] T. Feng, K.M. Kozloff, G. Xu, S. Du, J. Yuan, C.X. Deng, X. Wang, Characterization of bone microstructure using photoacoustic spectrum analysis, in: A.A. Oraevsky, L.V. Wang (Eds.), San Francisco, California, United States, (2015) 93234I. https://doi.org/10.1117/12.2078258.

[27] T. Feng, K.M. Kozloff, C. Tian, J.E. Perosky, Y.-S. Hsiao, S. Du, J. Yuan, C.X. Deng, X. Wang, Bone assessment via thermal photo-acoustic measurements, Opt. Lett. 40 (2015) 1721–1724, https://doi.org/10.1364/OL.40.001721.

[28] W. Xie, T. Feng, M. Zhang, J. Li, D. Ta, L. Cheng, Q. Cheng, Wavelet transform-based photoacoustic time-frequency spectral analysis for bone assessment, Photoacoustics 22 (2021), 100259, https://doi.org/10.1016/j.pacs.2021.100259.

[29] S. Huang, Y. Qin, Y. Chen, J. Pan, C. Xu, D. Wu, W.-Y. Chao, J.T. Wei, S.A. Tomlins, X. Wang, J.B. Fowlkes, P.L. Carson, Q. Cheng, G. Xu, Interstitial assessment of aggressive prostate cancer by physio-chemical photoacoustics: an *ex vivo* study with intact human prostates, Med. Phys. 45 (2018) 4125–4132, https://doi.org/10.1002/mp.13061.

[30] S. Wu, Y. Chen, S. Huang, C. Xu, D. Wu, Q. Cheng, Photoacoustic spectrum analysis for quick identification and grading of prostate cancer. 2020 IEEE International Ultrasonics Symposium (IUS), IEEE,, Las Vegas, NV, USA, 2020, pp. 1–4, https://doi.org/10.1109/IUS46767.2020.9251610.

[31] Yingna Chen#, Chengdang Xu#, Zhaoyu Zhang, Anqi Zhu, Xixi Xu, Jing Pan, Ying Liu, Denglong Wu, Shengsong Huang, Qian Cheng, Prostate cancer identification via photoacoustic spectroscopy and machine learning, Photoacoustics 23 (2021), 100280, https://doi.org/10.1016/j.pacs.2021.100280.

[32] I. Daubechies, The wavelet transform, time-frequency localization and signal analysis, IEEE Trans. Inf. Theory 36.5 (1990) 961–1005, https://doi.org/10.1063/1.4928520.

[33] J.N. Watson, P.S. Addison, G.R. Clegg, M. Holzer, F. Sterz, C.E. Robertson, A novel wavelet transform based analysis reveals hidden structure in ventricular fibrillation, Resuscitation 43 (2000) 121–127, https://doi.org/10.1016/S0300-9572(99)00127-6.

[34] M.P. Wachowiak, D.C. Hay, M.J. Johnson, Assessing heart rate variability through wavelet-based statistical measures, Comput. Biol. Med. 77 (2016) 222–230, https://doi.org/10.1016/j.compbiomed.2016.07.008.

[35] O. Faust, R. Acharya U, S. Krishnan, L.C. Min, Analysis of cardiac signals using spatial filling index and time-frequency domain, BioMed. Eng. OnLine 3 (2004) 30, https://doi.org/10.1186/1475-925X-3-30.

[36] O. Abdi Monfared, A. Doroudi, A. Darvishi, Diagnosis of rotor broken bars faults in squirrel cage induction motor using continuous wavelet transform, COMPEL 38 (2019) 167–182, https://doi.org/10.1108/COMPEL-11-2017-0487.

[37] Z. Huo, Y. Zhang, P. Francq, L. Shu, J. Huang, Incipient fault diagnosis of roller bearing using optimized wavelet transform based multi-speed vibration signatures, IEEE Access 5 (2017) 19442–19456, https://doi.org/10.1109/ACCESS.2017.2661967.

[38] M. Kulesh, M. Holschneider, M.S. Diallo, Geophysical wavelet library: applications of the continuous wavelet transform to the polarization and dispersion analysis of signals, Comput. Geosci. 34 (2008) 1732–1752, https://doi.org/10.1016/j.cageo.2008.03.004.

[39] G.R.J. Cooper, D.R. Cowan, Blocking geophysical borehole log data using the continuous wavelet transform, Explor. Geophys. 40 (2009) 233–236, https://doi.org/10.1071/EG08127.

[40] R.B. Perez, J.K. Mattingly, J.S. Perez, Wavelet Transform Techniques and Signal Analysis, (1993).

[41] Y. LeCun, Y. Bengio, G. Hinton, Deep learning, Nature 521 (2015) 436–444, https://doi.org/10.1038/nature14539.

[42] Q. Li , W. Cai , X. Wang , Y. Zhou , D.D. Feng , M. Chen , Medical image classification with convolutional neural network 2014 13th International Conference on Control Automation Robotics & Vision (ICARCV) 2014 IEEE, Singapore 844 848 doi: 10.1109/ICARCV.2014.7064414.

[43] T.-H. Chan, K. Jia, S. Gao, J. Lu, Z. Zeng, Y. Ma, PCANet: a simple deep learning baseline for image classification? IEEE Trans. Image Process 24 (2015) 5017–5032, https://doi.org/10.1109/TIP.2015.2475625.

[44] A. Krizhevsky, I. Sutskever, G.E. Hinton, ImageNet classification with deep convolutional neural networks, Commun. Acm. 60 (2017) 84–90, https://doi.org/10.1145/3065386.

[45] S. Yu, S. Jia, C. Xu, Convolutional neural networks for hyperspectral image classification, Neurocomputing 219 (2017) 88–98, https://doi.org/10.1016/j.neucom.2016.09.010.

[46] C. Dong, C.C. Loy, K. He, X. Tang, Image super-resolution using deep convolutional networks, IEEE Trans. Pattern Anal. Mach. Intell. 38 (2016) 295–307, https://doi.org/10.1109/TPAMI.2015.2439281.

[47] J. Kim, J.K. Lee, K.M. Lee, Accurate Image Super-Resolution Using Very Deep Convolutional Networks, ArXiv:1511.04587 [Cs]. (2016). ⟨http://arxiv.org/abs/1511.04587⟩ (accessed December 2, 2021).

[48] Y. Zhang , Y. Tian , Y. Kong , B. Zhong , Y. Fu , Residual Dense Network for Image Super-Resolution 2018 IEEE/CVF Conference on Computer Vision and Pattern Recognition 2018 IEEE, Salt Lake City, UT 2472 2481 doi: 10.1109/CVPR.2018.00262.

[49] K. He , X. Zhang , S. Ren , J. Sun , Deep Residual Learning for Image Recognition 2016 IEEE Conference on Computer Vision and Pattern Recognition (CVPR) 2016 IEEE, Las Vegas, NV, USA 770 778 doi: 10.1109/CVPR.2016.90.

[50] P.A. Humphrey, H. Moch, A.L. Cubilla, T.M. Ulbright, V.E. Reuter, The 2016 WHO classification of tumours of the urinary system and male genital organs—part B: prostate and bladder tumours, Eur. Urol. 70 (2016) 106–119, https://doi.org/10.1016/j.eururo.2016.02.028.

[51] A.V. D'amico, R. Whittington, S.B. Malkowicz, D. Schultz, K. Blank, G.A. Broderick, J.E. Tomaszewski, A.A. Renshaw, I. Kaplan, C.J. Beard, A. Wein, Biochemical outcome after radical prostatectomy, external beam radiation therapy, or interstitial radiation therapy for clinically localized prostate cancer, JAMA 280 (1998) 969–974.

[52] B.E. Treeby, B.T. Cox, k-Wave: MATLAB toolbox for the simulation and reconstruction of photoacoustic wave fields, J. Biomed. Opt. 15 (2010), 021314, https://doi.org/10.1117/1.3360308.

[53] H.-W. Wang, N. Chai, P. Wang, S. Hu, W. Dou, D. Umulis, L.V. Wang, M. Sturek, R. Lucht, J.-X. Cheng, Label-free bond-selective imaging by listening to vibrationally excited molecules, Phys. Rev. Lett. 106 (2011), 238106, https://doi.org/10.1103/PhysRevLett.106.238106.

[54] H. Lei, L.A. Johnson, S. Liu, D.S. Moons, T. Ma, Q. Zhou, M.D. Rice, J. Ni, X. Wang, P.D.R. Higgins, G. Xu, Characterizing intestinal inflammation and fibrosis in Crohn's disease by photoacoustic imaging: feasibility study, Biomed. Opt. Express 7 (2016) 2837–2848, https://doi.org/10.1364/BOE.7.002837.

[55] R. George, L.J. Walsh, Performance assessment of novel side firing flexible optical fibers for dental applications: NOVEL SIDE FIRING FLEXIBLE OPTICAL FIBERS, Lasers Surg. Med. 41 (2009) 214–221, https://doi.org/10.1002/lsm.20747.

[56] X. Ou, P. Yan, Y. Zhang, B. Tu, G. Zhang, J. Wu, W. Li, Moving object detection method via resnet-18 with encoder–decoder structure in complex scenes, IEEE Access 7 (2019) 108152–108160, https://doi.org/10.1109/ACCESS.2019.2931922.

[57] C. Han, Y. Duan, X. Tao, J. Lu, Dense convolutional networks for semantic segmentation, IEEE Access 7 (2019) 43369–43382, https://doi.org/10.1109/ACCESS.2019.2908685.

[58] L. Fan, H. Kong, W.-C. Wang, J. Yan, Semantic segmentation with global encoding and dilated decoder in street scenes, IEEE Access 6 (2018) 50333–50343, https://doi.org/10.1109/ACCESS.2018.2868801.
[59] Peng Shi Qi Zhou, Shengyuan Xu Honghai Liu, Neural-network-based decentralized adaptive output-feedback control for large-scale stochastic nonlinear systems, IEEE Trans. Syst. Man, Cybern. B 42 (2012) 1608–1619, https://doi.org/10.1109/TSMCB.2012.2196432.
[60] J. Long , E. Shelhamer , T. Darrell , Fully convolutional networks for semantic segmentation Pro. IEEE Conf. Comput. Vis. Pattern Recogn. 2015 3431 3440 doi: 10.1109/CVPR.2015.7298965.
[61] C. Morrison, J. Thornhill, E. Gaffney, The connective tissue framework in the normal prostate, B.P.H and prostate cancer: analysis by scanning electron microscopy after cellular digestion, Urol. Res. 28 (2000) 304–307, https://doi.org/10.1007/s002400000123.
[62] Y. Pu, W. Wang, G. Tang, R.R. Alfano, Changes of collagen and nicotinamide adenine dinucleotide in human cancerous and normal prostate tissues studied using native fluorescence spectroscopy with selective excitation wavelength, J. Biomed. Opt. 15 (2010), 047008, https://doi.org/10.1117/1.3463479.
[63] A. Llorente, T. Skotland, T. Sylvänne, D. Kauhanen, T. Róg, A. Orłowski, I. Vattulainen, K. Ekroos, K. Sandvig, Molecular lipidomics of exosomes released by PC-3 prostate cancer cells, Biochim. Et. Biophys. Acta (BBA) Mol. Cell Biol. Lipids 1831 (2013) 1302–1309, https://doi.org/10.1016/j.bbalip.2013.04.011.
[64] X. Wu, G. Daniels, P. Lee, M.E. Monaco, Lipid metabolism in prostate cancer, Am. J. Clin. Exp. Urol. 2 (2014) 111–120.

Shiying Wu is a Ph.D. candidate student from Institute of Acoustics, School of Physics Science and Engineering of Tongji University. She received Bachelor degree from Tongji University. Her current research focuses on Photoacoustic spectrum analysis and Photoacoustic imaging.

Ying Liu received the M.M. degree from Shanghai Jiao Tong University in 2010 and is currently a M.D. student in the Department of Urology at Tongji Hospital of Tongji University at Shanghai, China. She studies mainly in the basic prostate research and photoacoustic prostate diagnosis and evaluation.

Yingna Chen is currently a Ph.D. student in the Institute of Acoustics of School of Physics Science and Engineering at Tongji University at Shanghai, China. Her research interests are in the clinical translation of photoacoustic imaging and spectrum analysis.

Chengdang Xu is currently a Ph.D. student in the Department of Urology at Tongji Hospital of Tongji University at Shanghai, China. His research interests are in the basic prostate research and photoacoustic prostate diagnosis and evaluation.

Panpan Chen is currently pursuing the M.S. degree with the Institute of Acoustics, Tongji University, China. Her current research interests include photoacoustic image reconstruction, bone imaging and deep learning.

Mengjiao Zhang is a Ph.D. candidate student from Institute of Acoustics, School of Physics Science and Engineering of Tongji University. She received Bachelor degree from Ocean University of China. Her current research focuses on photoacoustic measurement of microvascular evaluation and photoacoustic imaging.

Wanli Ye is currently a master student in the Institute of Acoustics of School of Physics Science and Engineering at Tongji University at Shanghai, China. He studies mainly in the photoacoustic signal analysis.

Denglong Wu received the Ph.D. degree in Medicine from Shanghai Medical University (now School of Medicine at Fudan University) in 1998. He is currently the senior attending of urology at Tongji Hospital and a professor at Tongji Univeristy. He has been dedicated to the basic research prostate cancer and clinical diagnosis and treatment of it.

Shengsong Huang received the B.S. degree from Soochow University in 2005 and received his Ph.D. from Tongji University in 2019. He served as junior attending at Tongji Hospital. His work focuses on prostate cancer diagnosis and evaluation through photoacoustic imaging and spectrum analysis.

Qian Cheng received the B.S. degree in physics, M.S. and PhD degree in acoustics from Tongji University, China, in 2000, 2003 and 2006, respectively. She is currently a professor at Tongji University. Since 2006, her research interests were optoacoustic phenomena, near- eld acoustic imaging technique, Schlieren imaging technique and the development of the acoustic detecting instruments. Her most recent research has focused on the clinical translation of photoacoustic imaging and quantitative analysis, and in particular for tumor diagnosis and evaluation.